How pulse energy affects ignition efficiency of DBD plasma-assisted combustion

How pulse energy affects ignition efficiency of DBD plasma-assisted combustion

OPEN ACCESS
IOP Publishing
Journal of Physics D: Applied Physics
J. Phys. D: Appl. Phys. **57** (2024) 025501 (15pp)
https://doi.org/10.1088/1361-6463/acf942

How pulse energy affects ignition efficiency of DBD plasma-assisted combustion

Ravi Patel[1,2,*], Rik Peelen[1], Jeroen van Oijen[2], Nico Dam[2] and Sander Nijdam[1]

[1] Department of Applied Physics, Eindhoven University of Technology, PO Box 513, 5600 MB Eindhoven, The Netherlands
[2] Department of Mechanical Engineering, Eindhoven University of Technology, PO Box 513, 5600 MB Eindhoven, The Netherlands

E-mail: r.b.patel@tue.nl

Received 26 May 2023, revised 1 September 2023
Accepted for publication 13 September 2023
Published 12 October 2023

Abstract

This work aims to find how coupled energy per pulse influences the ability of a pulsed dielectric barrier discharge (DBD) plasma to ignite fuel-lean methane–air flow. For that, experiments are performed on a custom-built DBD flow reactor with a variable dielectric thickness and the discharge is operated by bursts of 10 ns duration pulses at 3 kHz repetition rate. With an increase in dielectric thickness, we observe that the coupled energy per pulse decreases even though applied voltage conditions are similar and so more pulses are required to ignite the lean mixture. Interestingly, we observe a significant increase in the minimum ignition energy (*MIE*) with an increase in the thickness beyond 3 mm. Moreover, the ignition kernel growth rate is much slower in the thicker dielectric cases even though total energy coupling per burst is similar. This phenomenon is investigated further by evaluating plasma parameters using electrical and optical diagnostics. Effective dielectric capacitance, discharge current, and voltage drop across the gas gap are derived from an equivalent circuit analysis, whereas plasma gas temperature and effective reduced electric field (E/N) are estimated from optical emission spectroscopy. From these analyses, we conclude that a thicker dielectric limits the discharge current and so the plasma filament temperature. For more than 3 mm thick dielectric cases, the filament heating per pulse is too low to achieve strong enough plasma pulse-to-pulse coupling which eventually leads to higher *MIE* and slower ignition kernel growth rate or the inability to ignite at all.

Keywords: plasma-assisted combustion, pulsed DBD plasma, DBD equivalent circuit model, optical emission spectroscopy, minimum ignition energy

* Author to whom any correspondence should be addressed.

1. Introduction

Plasma-assisted ignition and flame stabilization in fuel-lean conditions has gained a lot of attention from both the plasma and combustion communities [1]. Flame temperature, soot, CO, and NO_x emissions are lower in fuel-lean conditions compared to stoichiometric or rich conditions making combustion cleaner [2]. However, ignition and flame stabilization are challenging in such lean conditions. Plasma can support lean combustion by providing heat and radicals on very short timescales ($\sim$ns $-$ μs) [3, 4]. Fast plasma processes give an edge to plasma-assisted combustion (PAC) over conventional flame stabilization mechanisms such as flow re-circulation by a bluff body or swirl, pilot flame stabilization, etc especially in high-speed propulsion engines such as scramjets and turbojets [5–9]. Another advantage of PAC is that it can have a higher energy efficiency of radical production than conventional thermal heating. This is achieved in non-equilibrium plasmas by selectively putting energy in electronic excitation and dissociation reactions. Electron energy loss fractions in various non-equilibrium processes depend on the electron energy distribution function which is governed by the reduced electric field (E/N, where E is the electric field and N is the gas number density) [10]. When using PAC, the plasma energy efficiency is especially important for domestic applications such as heating or power generation [11, 12].

Traditionally, dielectric barrier discharges (DBDs) are known for generating low-temperature non-equilibrium plasmas [13]. A DBD has at least one dielectric barrier between the electrodes to restrict the current and prevent the transition to a spark. The dielectric acts as a capacitor that can store a maximum charge of $Q = C_D \cdot V_D$, where, C_D is the dielectric capacitance and V_D the voltage drop over the capacitor. The current stops at the maximum charging point and so does the plasma. Hence, DBDs can only be operated by alternating or pulsed electric fields. DBDs can have various types of electrode constructions such as volume, surface, coplanar, capillary, jet, etc [13, 14]. Typically, discharges occur in the form of micro-discharges at near atmospheric or higher pressure conditions [15, 16]. It is possible to generate a diffuse plasma in pure gases like helium, neon, nitrogen, etc even at atmospheric pressure by slowing down the breakdown and avoiding the formation of rapid electric field gradients [17–19]. DBDs are used for various chemical processes such as ozone generation [20], water treatment [21], CO_2 dissociation [22] and dry methane reforming [23]. The ability to generate radicals and active species at lower plasma temperatures than fuel auto-ignition temperatures makes DBDs suitable for combustion applications. DBDs have been studied to enhance ignition [24, 25] and flame stabilization [26–28] in various operating conditions and types of flames.

Recent developments in pulsed power technology have made nanosecond pulsed power supplies available. Nanosecond duration repetitively pulsed (NRP) discharges have high energy loading at relatively high E/N [29, 30]. At near atmospheric pressure, NRP discharges can be in corona, glow, non-equilibrium spark, or equilibrium spark regime depending on operating conditions and electrode construction [31, 32]. Typically, it is difficult to maintain a plasma in one specific regime, as small changes in the operating conditions can modify the plasma regime [33]. Especially the non-equilibrium spark to equilibrium spark transition is very fast. Minesi *et al* have observed this transition within one pulse [34]. The equilibrium spark regime can be avoided by using NRP discharges with a dielectric barrier.

NRP discharge assisted ignition with and without dielectric barrier has been studied by various researchers, using pin-to-pin NRP spark discharge [35–38], pulsed corona discharge [39–41], pulsed surface DBD [25, 42] and NRP diffused DBD [43–45]. Lou *et al* [43] have shown that it is possible to achieve low-temperature ignition of hydrocarbon-air flows at low pressure ($\sim$100 mbar) using a NRP-operated DBD. In our previous work, we have shown the possibility of igniting methane–air flows at near atmospheric conditions using NRP-operated DBDs while maintaining filament temperatures clearly below the auto-ignition temperature [46, 47]. We highlighted the importance of plasma pulse-to-pulse coupling for ignition. Also, we characterized the effects of flow speed and pulse repetition rate (PRR) on the pulse-to-pulse coupling [48]. Our previous studies [46, 48] are performed on the same DBD reactor as in this work, with 5 mm discharge gap and one electrode covered with a 2 mm thick dielectric. Along with these reported studies, we have tried reactor configurations with both electrodes covered with a 2 mm thick dielectric. Even though we were able to ignite plasma, we could not achieve methane–air ignition which motivated us to perform the parametric study reported here.

In this work, we aim to investigate the influence of the dielectric and most importantly its thickness (d) on the plasma pulse-to-pulse coupling and thereby its ability to ignite methane–air flows. The maximum charge storing capacity (Q) is proportional to C_D which is inversely proportional to d. This means that plasma energy coupling should reduce with increasing d for constant applied voltages. In this way, we study the effect of plasma energy on the ignition and find the minimum ignition energy (*MIE*). Along with dielectric thickness, a parametric study is performed for various pressures and the number of pulses per burst while flow speed and equivalence ratio are kept constant so that hypotheses on the effect of dielectric thickness can be verified. Systematic optical and electric diagnostics are performed for varying dielectric thickness. Firstly, we discuss the plasma morphology and ignition probability evaluated from high-speed imaging. Then, the results from electrical measurements and the equivalent circuit analysis are presented. This provides information on plasma energy per pulse, dielectric capacitance (C_D), discharge current (I_R), and gas gap voltage (V_G). Lastly, we highlight plasma properties such as gas temperature, reduced electric field, and electron density determined from optical emission spectroscopy (OES).

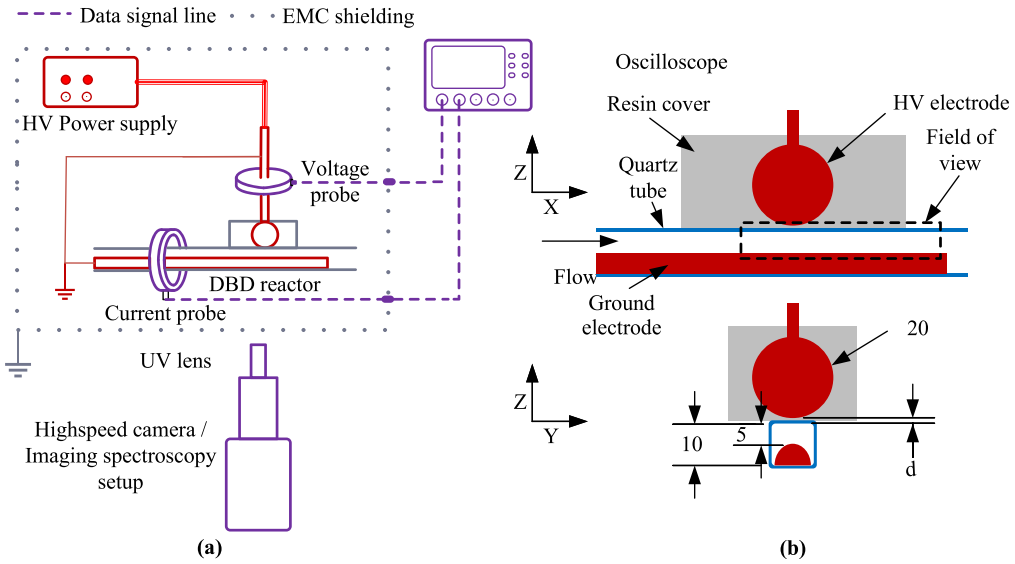

Figure 1. (a) Schematics of the experimental setup and (b) schematics cross-section views from two sides of the DBD reactor (all dimensions are in mm) [46]. Reproduced from [48]. © R Patel, J van Oijen, S Nijdam, and N Dam). Published by IOP Publishing Ltd. CC BY 4.0.

2. Experimental setup and methods

2.1. Experimental setup

In this work we use the experimental setup that was extensively described in a previous paper [46]. Schematics of the overall setup along with cross-sectional views of the main reactor are shown in figure 1. The main reactor consists of a quartz flow channel with a DBD arrangement. A ball-shaped high-voltage (HV) electrode is embedded inside a resin and placed over the quartz tube. A semi-cylindrical rod is placed inside the quartz tube and is connected to ground. This arrangement leaves a 5 mm minimum discharge gap through which air or a methane–air mixture flows. The quartz tube and resin layer act as a dielectric. The quartz wall thickness is 0.9 ($\pm$0.1) mm and the resin layer thickness is varied in order to study the effect of dielectric thickness. The minimum resin layer thicknesses (at the axis of the HV electrode) studied in this work are 1, 2, 4, 6, and 8 mm. The resin layer thickness is controlled by embedding HV electrode using a custom-made mold in which the ball distance from the bottom surface of the mold can be controlled with about $\pm$0.2 mm accuracy. For simplicity, these cases are referred to by their approximate total thicknesses (d) which are 2, 3, 5, 7, and 9 mm respectively.

The DBD is operated using pulses of approximately 10 ns, with a peak voltage of around 30 kV and a PRR of 3 kHz, derived from a Megaimpulse NPG-3500 power supply. Samples of voltage and current waveforms are shown in figure 2. The flow system is built such that mass flow rate and pressure can be varied independently. All measurements are performed in burst mode at a fixed 90 Hz burst frequency, 3 kHz PRR, and 1.5 m s^{-1} flow speed, whereas the number of pulses per burst (n_b) and pressure (p) are varied. The 110 ms between bursts is longer than the residence time of the gas between the electrodes, so individual bursts are independent of each other. The pulse number in a burst is denoted as n_p which ranges from 1 to n_b (the total number of pulses per burst).

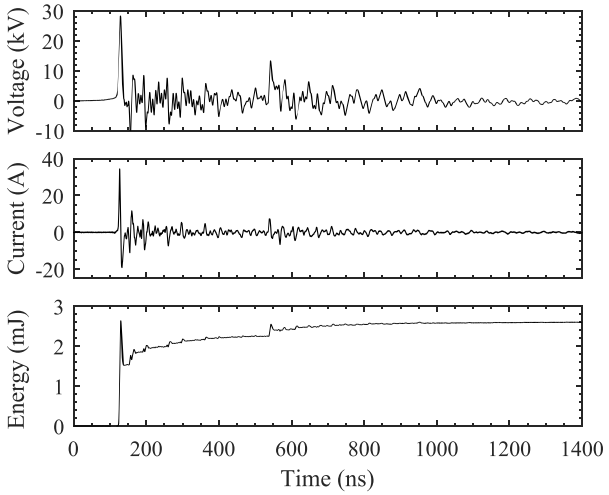

Figure 2. Voltage, current, and energy waveforms of an air plasma at $p = 700$ mbar and for $d = 2$ mm. $n_b = 10$, and $n_p = 7$. Waveforms are averaged over 50 pulses.

2.2. Diagnostic methods

2.2.1. High-speed visualization. A combination of a Photron SA-X3 high-speed camera and a La-Vision high-speed intensifier (IRO) is used for the visualization measurements. The measurements are performed in two ways: the first is to capture pulse-to-pulse plasma images. For that, the camera frame rate and intensifier gate delay are set such

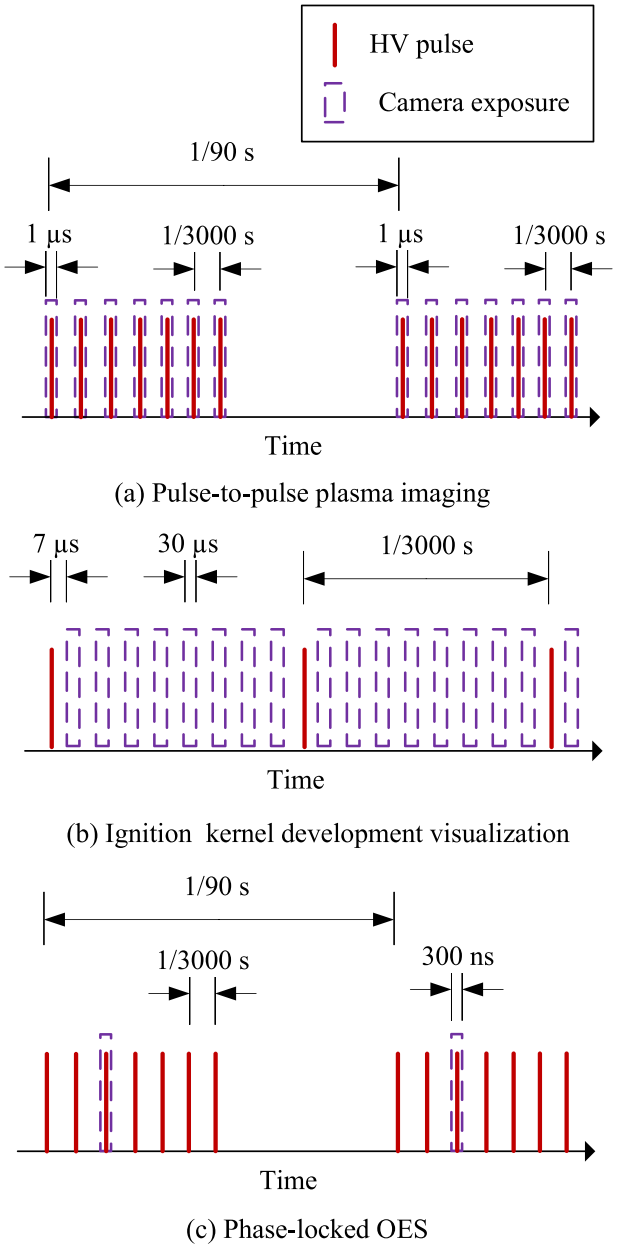

Figure 3. Schematics of timing diagram for various diagnostics (a) pulse-to-pulse plasma imaging at burst frequency = 90 Hz, PRR = 3 kHz, $n_b = 7$, and camera exposure = 1 μs, (b) ignition kernel development visualization at PRR = 3 kHz, camera frame-rate = 24 kHz and camera exposure = 30 μs, and (c) phase-locked OES at burst frequency = 90 Hz, PRR = 3 kHz, $n_b = 7$, $n_p = 3$, and camera exposure = 300 ns. Reproduced from [46]. CC BY 4.0.

that emission from a single plasma pulse is captured in each frame. The camera gate is set to 1000 ns, which is long enough to capture all of the plasma optical emission. The second way of measurement is to visualize ignition kernel development in methane–air flows. Camera and plasma timings are set such that only combustion chemiluminescence is captured by skipping the time period with most plasma emission. A 30 μs gate is used in this case. Schematics of the timing diagram for both types of measurement are shown in figure 3 and the detailed description can be found in our previous paper [46].

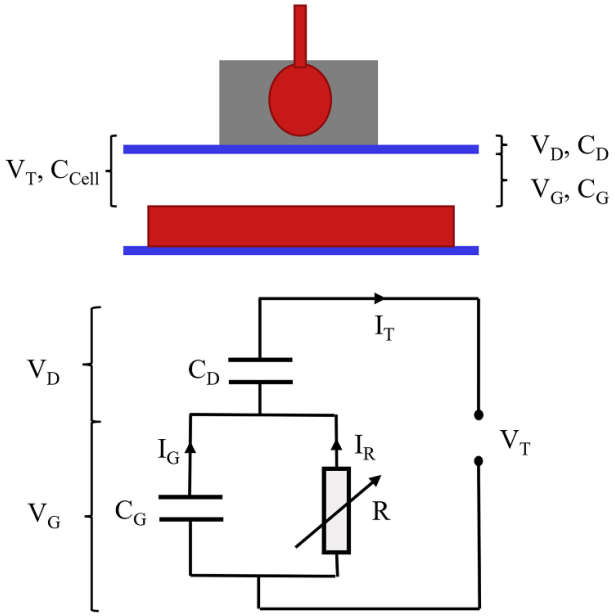

Figure 4. A schematics of the equivalent circuit description of the DBD reactor. Nomenclature is described in the text.

2.2.2. Electrical diagnostics and equivalent circuit analysis. Instantaneous applied voltage (V_T) and current (I_T) waveforms are measured using a homemade D-dot sensor [49] and an AMS CT-F 1.0 S current probe. As shown in figure 1(a), the current probe is placed at the ground side such that current flowing through the discharge region can be measured and interference from most of the parasitic current can be avoided. The voltage and current probes have bandwidths of about 1 GHz and 500 MHz respectively. Both waveforms are recorded using a Lecroy 400 MHz oscilloscope at 5 gigasamples per second. Along with voltage and current sample waveforms, a resulting energy waveform is also plotted in figure 2. The energy (E_T) is calculated using:

$$E_T(t) = \int V_T(t) \cdot I_T(t)\ \mathrm{d}t. \tag{1}$$

About 1.8 mJ is coupled in by the main pulse which increases to about 2.8 mJ after about one microsecond due to reflections of the pulse in the electrical system.

The measured current is the total current and includes both capacitive and resistive components. The resistive component is the discharge current whereas most of the capacitive part reflects back from the reactor. Therefore, the instantaneous energy calculated using equation (1) has a peak of about 2.8 mJ which reduces to 1.8 mJ once capacitive energy has reflected. An equivalent circuit analysis is performed to derive discharge current (I_R), voltage drop across gas gap (V_G), and discharge power (P_R) [50–52].

A schematic of the used equivalent circuit of the DBD reactor is shown in figure 4. Here, the dielectric (quartz + resin) is represented as a capacitor with capacitance C_D. The gas gap is represented by a capacitor (C_G) in parallel with a variable resistor (R). The dielectric and gas gap are connected in series. C_{cell} is the reactor total capacitance without plasma

ignition. It is basically a series connection of the dielectric and gas gap capacitance:

$$\frac{1}{C_{\text{cell}}} = \frac{1}{C_{\text{D}}} + \frac{1}{C_{\text{G}}}. \tag{2}$$

From Kirchhoff's current law, the resistive current (I_{R}) and voltage drop across the gas gap (V_{G}) can be derived [50]:

$$I_{\text{R}}(t) = \frac{1}{1 - \frac{C_{\text{cell}}}{C_{\text{D}}}} \left(I_{\text{T}}(t) - C_{\text{cell}} \cdot \frac{\mathrm{d}V_{\text{T}}(t)}{\mathrm{d}t} \right), \tag{3}$$

$$V_{\text{G}}(t) = V_{\text{T}}(t) - \frac{\int I_{\text{T}}(t)\ \mathrm{d}t}{C_{\text{D}}}. \tag{4}$$

These equations depend on the parameters which can be measured directly or derived from the measured parameters.

Typically, as per (2), C_{cell} depends on C_{D} and C_{G} but they are also unknown and therefore C_{cell} is estimated using

$$I_{\text{T}}(t) = C_{\text{cell}} \cdot \frac{\mathrm{d}V_{\text{T}}(t)}{\mathrm{d}t}, \tag{5}$$

which is acquired under conditions where no discharge occurs. Thus, C_{cell} is estimated as the ratio of the peak value of I_{T} and the peak of the time derivative of V_{T}.

C_{D} is evaluated from QV plots as described by Pipa *et al* [53, 54]. Equation (4) can be rewritten as

$$Q_{\text{max}} = C_{\text{D}} \cdot (V_{\text{Qmax}} - V_{\text{res}}), \tag{6}$$

for the maximum charge condition at the dielectric surface. Here, Q_{max} represents the maximum charge and V_{Qmax} is the applied voltage at the time of maximum charge. V_{res} is the voltage drop across the gas gap at the maximum charge condition and should be close to the plasma extinction voltage. Therefore, V_{res} is assumed to be independent of the applied voltage. If the relation between Q_{max} and V_{Qmax} is linear for various applied voltages, then the slope of this line represents C_{D} as shown in figure 5. The slope of a linear fit through the maximum charging points represents $C_{\text{D}} = 7.2\,\text{pF}$ for 2 mm dielectric thickness.

2.2.3. Optical emission spectroscopy (OES). OES is performed in order to evaluate two plasma parameters: (1) gas temperature and (2) effective reduced electric field (E/N). An Acton instruments 500i imaging spectrograph is used along with a Roper Scientific PIMAX2 ICCD camera. Phase-locked measurements are performed, as shown in figure 3, using over 2000 shots for each parameter set with a 300 ns camera gate. A detailed description of the setup can be found in our previous work [46]. The spectrograph slit is kept perpendicular to the discharge gap so that plasma optical emission from 1.25 mm above the grounded electrode is collected.

The gas temperature can be assumed to be close to the rotational temperature of the $N_2(C)$ state [32, 55]. The rotational temperature of the $N_2(C)$ state is evaluated by fitting the $N_2(C \rightarrow B, \Delta\nu = 1)$ band around 380 nm. The fitting is performed using the MassiveOES tool as it allows batch processing of the spectra and it supplies fitting quality estimations [56, 57]. A sample of a measured spectrum with a fitted spectrum and residuals for the seventh pulse in an air plasma at 700 mbar with 3 mm dielectric thickness is shown in figure 6(a). An effective E/N is estimated from the intensity ratio of the emission from the $N_2(C \rightarrow B, 2-5)$ and N_2^+ $(B \rightarrow X, 0-0)$ transitions. Sample spectra of these transitions for various pulse numbers are shown in figure 6(b). The experimentally measured intensity ratio is correlated with E/N using the empirical relation given by Paris *et al* [58].

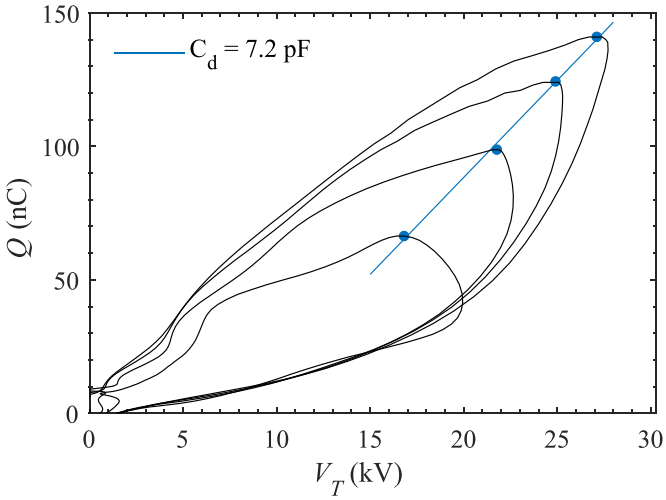

Figure 5. Charge vs applied voltage plot for the tenth pulse in a burst for $d = 2\,\text{mm}$, $n_{\text{p}} = 10$, $n_{\text{b}} = 10$, $p = 700\,\text{mbar}$ and various applied voltages.

3. Results and discussions

For all measurements, the gas (air or a methane–air mixture) flow speed and plasma burst frequency are fixed to $1.5\ \text{m s}^{-1}$ and 90 Hz. Parametric studies are performed for various dielectric thicknesses, pressures, and number of pulses per burst. As explained in the previous section, three major types of experiments are performed and the results are discussed below.

3.1. Pulse-to-pulse plasma morphology

Pulse-to-pulse air plasma images are shown in figure 7 for various dielectric thicknesses and pulse numbers at 700 mbar. Two burst cases for each thickness are shown. The $d = 2\,\text{mm}$ case has been extensively studied in our previous work [46]. For this case we observe strong pulse-to-pulse coupling from the second pulse onwards which changes the plasma morphology from distributed multiple weak filaments to a few strong filaments. In literature, this phenomenon is often referred to as 'plasma memory effect'. Long lived negative ions (such as O^-, O_2^-, O_3^-) [30, 59] or charges stored at the dielectric surface [60] provide initial free electrons for discharge initiation.

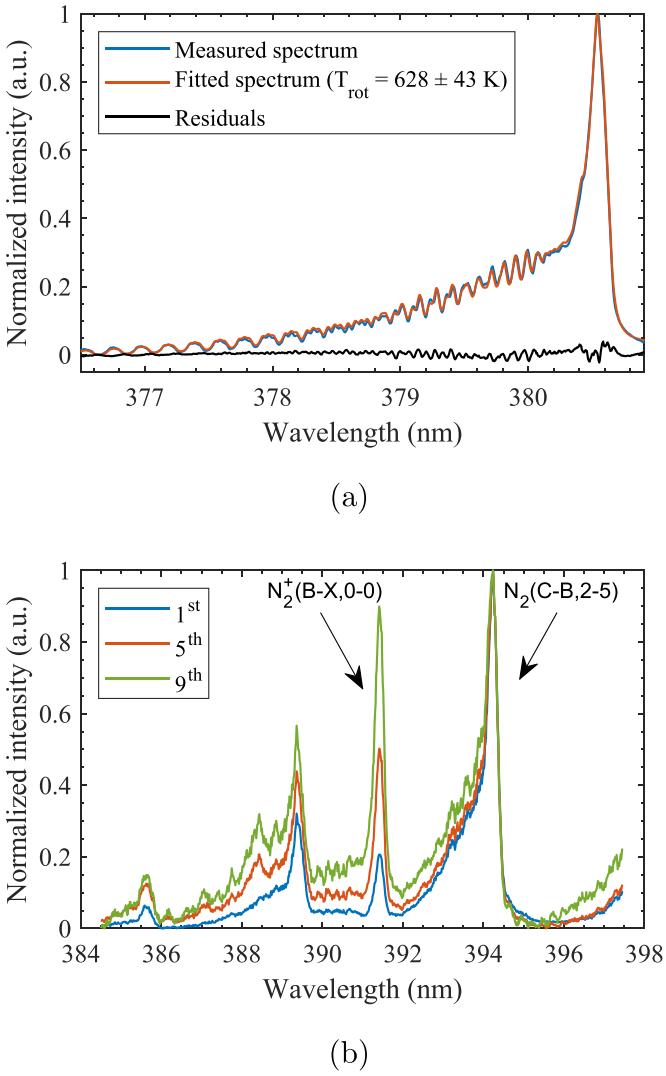

Figure 6. (a) Measured emission spectrum of air plasma with the fitted spectrum and residual at $d = 3$ mm, $n_p = 7$, $n_b = 10$, and $p = 700$ mbar, and (b) measured emission spectra of air plasma used for E/N estimations at $d = 3$ mm, $n_p = 1, 5, 9$, $n_b = 10$, and $p = 700$ mbar.

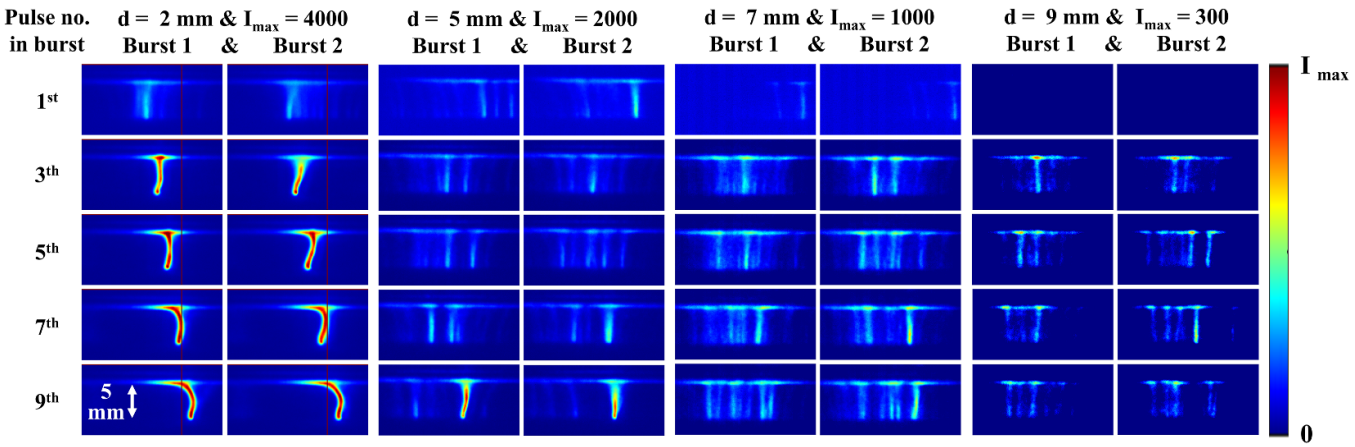

Figure 7. Pulse-to-pulse air plasma discharge images for various dielectric thicknesses at $p = 700$ mbar and $n_b = 10$. Two burst cases for each dielectric thickness are shown to get an impression of reproducibility. The intensity scale is varied per thickness setting. The flow direction is from left to right. The reds seen in the first two columns are due to the software error while storing the images.

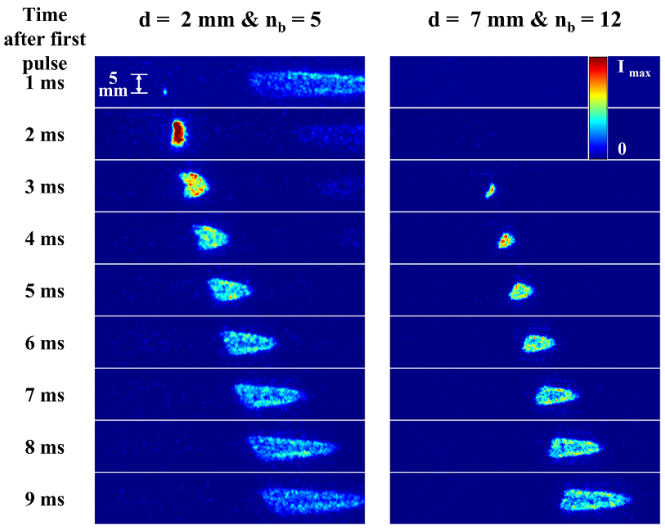

Figure 8. High-speed images of ignition kernel development in methane–air flows at $p = 700$ mbar and $d = 2$ mm with $n_b = 5$ (left panel burst duration 1.66 ms) or $d = 7$ mm with $n_b = 12$ (right panel burst duration 4 ms).

Once the discharge is initiated, it flows through the easier path created by the residual heat from the previous discharge.

We can observe that the plasma becomes less and less intense with an increase in dielectric thickness. At $d = 5$ mm, we observe multiple weak filaments up till five pulses and strong pulse-to-pulse coupling starting only from the ninth pulse. The pulse-to-pulse coupling is very weak for $d = 7$ mm, and no coupling is observed for $d = 9$ mm. We have reported similar behavior of weakening of the pulse-to-pulse coupling at higher flow speeds, lower PRR, and lower pressures [46, 48]. This was attributed to lower flow residence time inside the discharge region or lower plasma gas heating. We investigate this phenomenon in more detail below.

3.2. Lean methane–air mixture ignition probability (P_{ign})

In order to investigate the influence of dielectric thickness on plasma ability to ignite, a premixed methane–air mixture of 0.6 equivalence ratio is fed to the reactor. Combustion chemiluminescence imaging at high speed is performed for various parameters. Two sample image series for $d = 2$ and 7 mm are shown in figure 8. The number of pulses per burst is kept to 5 and 12, respectively. Similar to our previous reports, a small ignition kernel near the grounded electrode is observed first which leads to the development of a self-sustained ignition kernel. Contrary to the $d = 2$ mm case, no signal is detected up till 3 ms for $d = 7$ mm. This indicates that 6 pulses are not enough to ignite the methane–air mixture $d = 7$ mm. A small emission pocket is seen at 3 ms leading to successful ignition kernel development. From the image series consisting of more than 50 bursts, we have determined the number of bursts with successful ignition and from that the ignition probability. P_{ign} is the ratio between these two numbers and is expressed as percentage. This is done for various sets of dielectric thicknesses, number of pulses per burst, and pressures and the results are plotted in figure 9.

We observe an increase in the minimum number of pulses required for ignition for increasing dielectric thickness. At 700 mbar, a minimum of 4, 5, and 9 pulses is required to achieve over 90% successful ignition probability for 2, 3, and 5 mm thickness, respectively. A maximum of about 35% ignition probability is observed at $d = 7$ mm and ignition is not observed at all at $d = 9$ mm. These trends are consistent with the trend observed for pulse-to-pulse coupling in air plasma.

At lower pressures, more pulses are required for ignition for all dielectric thicknesses. We found 35% maximum ignition probability at $d = 7$ mm and 700 mbar which goes to zero at 500 mbar. Similarly, the 100% ignition probability at $d = 5$ mm and 700 or 500 mbar goes to nearly zero at 400 mbar. It is known that the MIE for methane is inversely proportional to pressure squared [61]. Moreover, we have reported a change in plasma morphology and less pulse-to-pulse plasma heating at reduced pressures. The combination of these phenomena can explain the ignition probability trends observed for lower pressures.

From the above measurements, it is evident that the plasma becomes weaker with increasing dielectric thickness and so does the plasma ability to ignite the methane–air mixture. In order to further characterize this phenomenon, we quantify the coupled energy per pulse and evaluate ignition efficiency in the next section. Subsequently, the effects of dielectric thickness on discharge current, the voltage drop across the gas gap, and discharge power are analyzed to gain more insights.

3.3. Electrical diagnostics

3.3.1. Energy coupled into plasma. The total energy coupled into the plasma is evaluated from the measured voltage and current waveforms using equation (1). The coupled energy during the first microsecond (using the timing shown in figure 2) for various peak voltages and dielectric thicknesses in an air plasma at 700 mbar is plotted in figure 10. This duration was chosen such that energy input due to reflections is also included in the plotted values. Each data cluster in figure 10 represents 2–10 pulse numbers of a burst at the same applied voltage condition from the power supply. Even though the applied voltage setting of the power supply is the same, the measured voltage in a cluster can vary a bit depending on the reactor impedance and PRR.

We measure about 1.5 kV higher voltages during the first pulses of each burst and energy coupling is less or equal to other pulses depending on whether the discharge is able to ignite or not. For simplicity, the first pulse data are not included in these plots; these are discussed in section 3.3.3. Moreover, each data point is a mean of over 50 waveforms captured at fixed operating conditions and pulse numbers. Two representative error bars are shown for $d = 2$ mm. The error is mostly dominated by imperfect phase matching of the voltage and current waveforms.

Two major trends from the plot can be highlighted. The first is that the energy coupling per pulse decreases with applied voltage. For $d = 2$ mm, the energy decreases from about 2.8 mJ

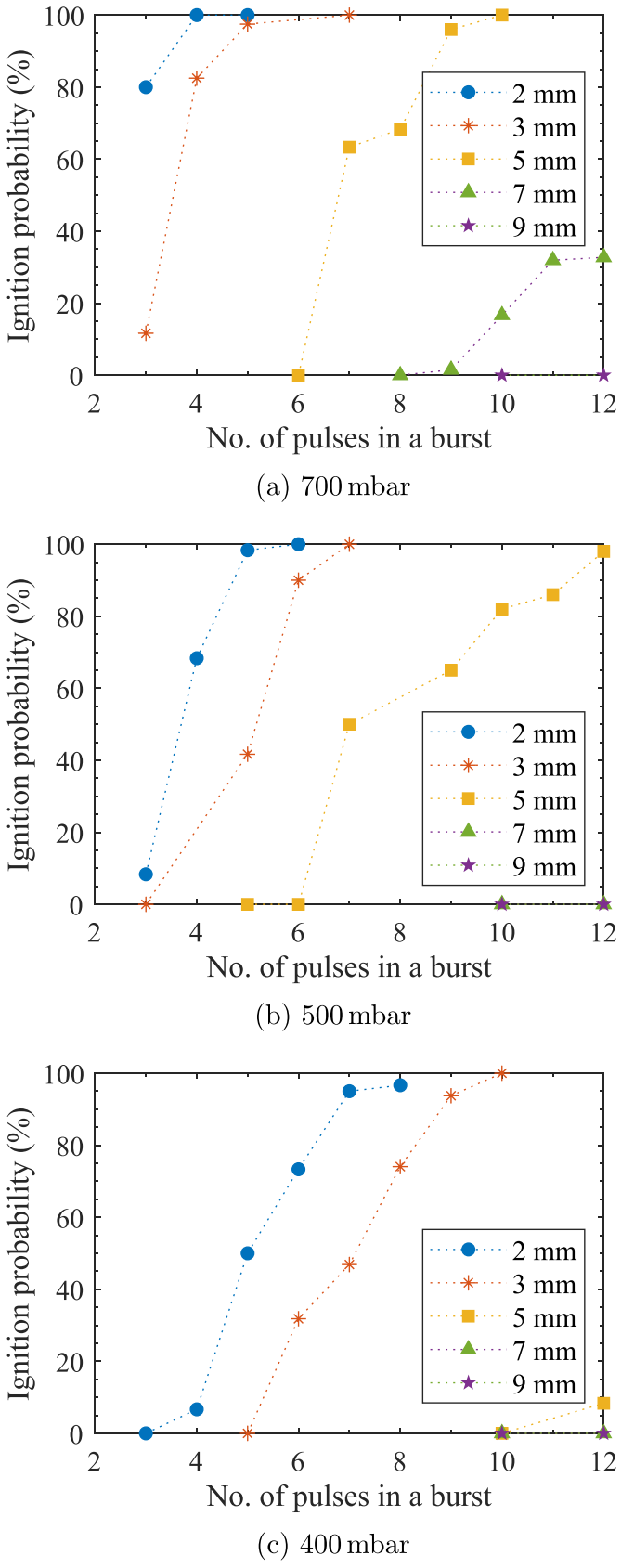

Figure 9. Successful ignition probabilities for various dielectric thicknesses and number of pulses per burst at 0.6 equivalence ratio and at (a) 700 mbar, (b) 500 mbar, and (c) 400 mbar pressures.

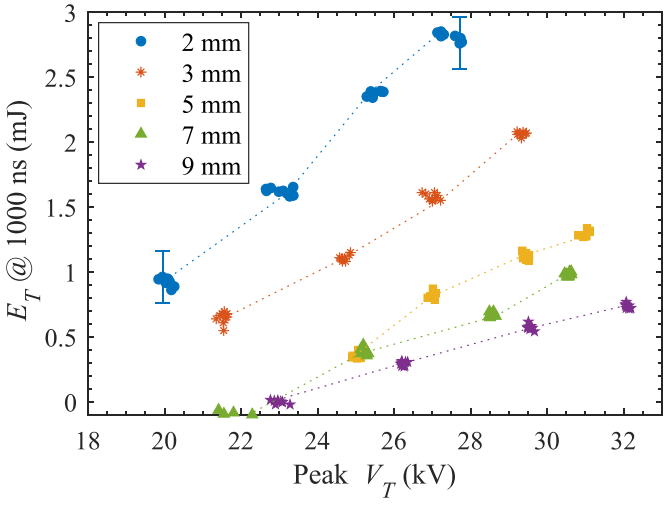

Figure 10. Energy coupled into an air plasma for various dielectric thicknesses and applied voltages at $n_b = 10$, $n_p = 2$–10, and $p = 500$ mbar. To avoid overcrowding, we have added only two error bars, but they are representative for all points.

per pulse at about 28 kV to about 0.8 mJ per pulse at 20 kV. The second trend is the energy coupling for thicker dielectrics is lower at similar applied voltages. The maximum energy coupling of about 2.8 mJ per pulse reduces by a factor of 4 to 0.7 mJ when increasing the dielectric thickness from 2 to 9 mm. Almost no energy is coupled in for thicker dielectrics at the lowest voltages which means that no plasma is ignited in these conditions.

The lower energy coupling for thicker dielectrics can explain the trends observed for plasma morphology and ignition probability in the previous sections. We evaluate *MIE* from equation (7)

$$MIE = n_{b(P_{ign}>80\%)} \cdot E_T, \tag{7}$$

where $n_{b(P_{ign}>80\%)}$ is a minimum number of pulses per burst needed to achieve more than 80% ignition probability and E_T is the total coupled energy in the burst. Table 1 includes *MIE* for various dielectric thicknesses and pressures. Moreover, the maximum total energies per burst studied in this work for not igniting conditions are summarized in table 2. The parametric study is performed up to $n_b = 14$ pulses so the total energy coupled during 14 pulses is the studied maximum energy per burst. It is expected that *MIE* increases as pressure is reduced for a given dielectric thickness [61].

Importantly, *MIE* increases significantly with the increase in the thickness for more than 3 mm, to the point at which ignition is not achieved even though total coupled energy is similar. In order to study the influence of energy per pulse on ignition kernel growth rate, the high-speed image series are processed using MatLab script, and the ignition kernel area for each time step is evaluated. The image processing steps are explained in our previous work [48]. The results are plotted in figure 11. The number of pulses per burst is also varied to keep the total energy coupling per burst similar (about 11 mJ) and

Table 1. Minimum ignition energy (*MIE*) in mJ for various dielectric thickness and pressure conditions. Conditions in which more than 80% ignition probability is not observed are represented as No Ign.

d	700 mbar	500 mbar	400 mbar
2	7.9	14.1	21.6
3	7.1	13.4	20.1
5	10.6	15.4	No Ign.
7	No Ign.	No Ign.	No Ign.
9	No Ign.	No Ign.	No Ign.

Table 2. Maximum energy per burst studied in this work for the conditions without 80% ignition probability.

d	700 mbar	500 mbar	400 mbar
5			25.5
7	8.3	12.3	16.7
9	3.6	8.6	9.9

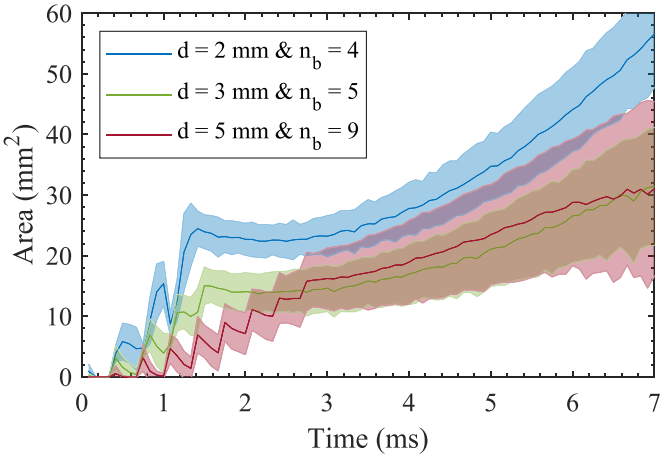

Figure 11. Ignition kernel growth rate for various dielectric thicknesses at 0.6 equivalence ratio and 700 mbar. The number of pulses per burst is also varied to keep the total energy coupling per burst almost constant. The mean areas and their standard deviations over 50 events are represented by the solid lines and shaded areas respectively.

the ignition probability at 100%. It is evident that the ignition kernel growth rate is much higher for 2 mm dielectric thickness than for thicker dielectrics. This means that a higher energy per pulse is beneficial for ignition kernel growth. Moreover, from our previous work [48], we know that the ignition kernel size is a function of total energy coupling per burst (i.e. the number of pulses per burst at fixed PRR multiplied with the energy per pulse) whereas in this work we observe the contrary. For thicker dielectrics, the pulse-to-pulse coupling is not observed for initial pulses of bursts so not all measured energy is contributing to ignition kernel development.

3.3.2. Dielectric capacitance (C_D) estimation. As we know, the energy coupling per pulse is directly related to the dielectric capacitance (C_D). The C_D values are estimated for all thickness cases using the method described in section 2.2.2.

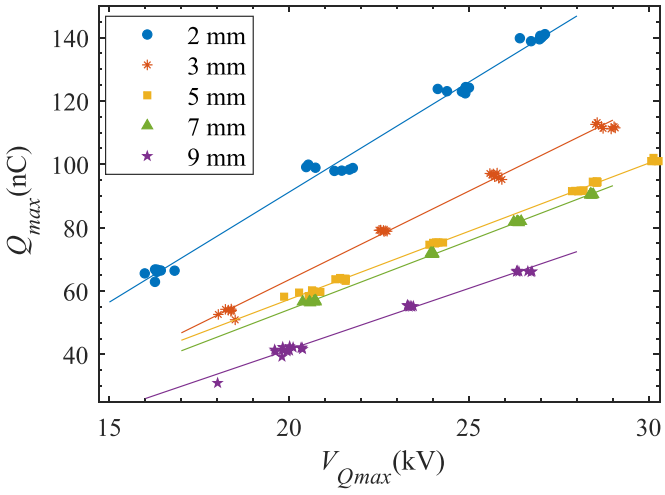

Figure 12. Maximum charge vs applied voltage at maximum charging for various dielectric thicknesses, and applied voltages at $p = 700$ mbar for $d = 2\,\&\,3$ mm and $p = 500$ mbar for $d = 5, 7\,\&\,9$ mm.

Table 3. Estimated C_D values for different dielectric thickness with their 95% confidence interval.

d	mean C_D (pF)	95% confidence interval (pF)
2	7.0	[6.7–7.2]
3	5.6	[5.4–5.8]
5	4.3	[4.3–4.4]
7	4.2	[4.2–4.3]
9	3.9	[3.7–4.0]

Sample plots of charge (Q) vs applied voltage (V_T) of the tenth pulses in air plasma for various applied voltages, 2 mm dielectric, and 700 mbar pressure are shown in figure 5. The slope of a linear fit through the maximum charging points represents C_D, here resulting in 7.2 pF. Similarly, Q_{max} vs V_{Qmax} for various applied voltages, pulse numbers, and dielectric thicknesses is shown in figure 12(b) along with fitted lines for each thickness. Four to ten pulse numbers ($n_p = 4$–10) are used for the calculations to ensure plasma breakdown with maximum charging of the dielectric. For the same reason, the experiments are performed also at a lower pressure (500 mbar) for thicker dielectrics (5, 7, and 9 mm). Here, an assumption is that the dielectric surface area covered by the charge stays the same with pressure. This is reasonable because the surface discharge over the dielectric surface is much bigger than the filament cross-sectional area at the studied pressures and the surface discharge is not expected to be perturbed much by the small pressure variation. The estimated effective C_D values are summarized in table 3.

3.3.3. Parameters derived from voltage, current, and energy waveforms. The resistive and capacitive components of the measured voltage and current waveforms are derived using estimated C_D and C_{cell} values calculated with equations (3) and (4). Voltage, current, and energy components of the first

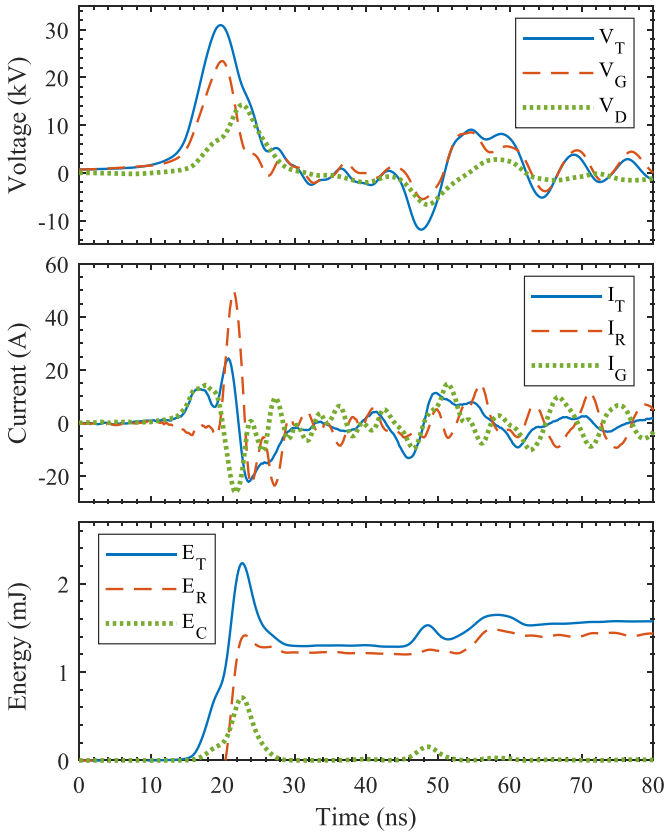

Figure 13. Voltage, current, and energy waveform components for $d = 2$ mm, $n_b = 10$, $n_p = 1$, and $p = 700$ mbar.

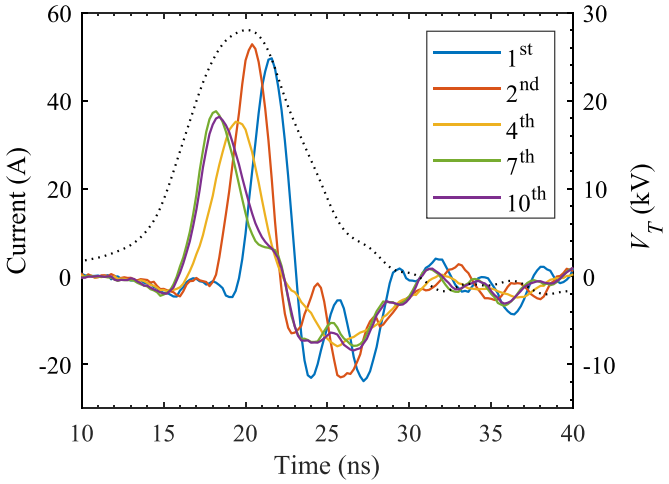

Figure 14. Examples of the resistive current component (I_R) for $d = 2$ mm, $n_b = 10$, $p = 700$ mbar, and various pulse numbers (n_p) in a burst. The V_T waveform is also included for reference (dotted black curve).

pulse of an air plasma at 700 mbar and 2 mm thick dielectric are shown in figure 13. The solid blue line is the measured voltage waveform V_T whereas the voltage drop over the gas gap V_G and over the dielectric V_D are shown with dashed red and dotted green lines, respectively. Initially, before the plasma breaks down, V_T is linearly divided over V_G and V_D. The division ratio depends on the values of C_G and C_D. After the 20 ns mark, V_G drops faster than V_T whereas V_D increases even though V_T decreases. Similarly, the capacitive current (I_C) initially follows I_T showing that the reactor works as a capacitor. At about the 20 ns mark, we see the occurrence of a resistive current (I_R) indicating plasma breakdown. After plasma breakdown, the gas gap resistance decreases and so does V_G. Because $V_D \propto Q$, V_D increases even though V_T decreases. Overall, this analysis gives information about V_G and I_R which cannot be measured directly. Discharge energy (E_R) is calculated by $\int V_G \cdot I_R \, dt$.

In order to visualize the pulse-to-pulse effects on the discharge properties, I_R waveforms for various pulse numbers, 2 mm dielectric thickness and 700 mbar are shown in figure 14. It is quite evident that plasma breakdown happens faster with increasing pulse number. The I_R peaks observed for the initial pulses (i.e. 1 & 2) are narrower and higher than peaks during later pulses (i.e. 7–10). From the pulse-to-pulse plasma visualization discussed in section 3.1, we know that the plasma filament occupies almost the same gas volume for consecutive pulses under these conditions. In the next section, we will show that this pulse-to-pulse behavior leads to an increase in gas temperature. This allows plasma ignition at lower V_T as the lower V_T is compensated by lower gas density.

The peak I_R and the time of the peak I_R for various pulse numbers and dielectric thicknesses are plotted in figure 15. The standard deviation over about 50 burst cases is shown as the error bar. It shows about 4% deviation in peak I_R. Even though we have assumed the surface discharge area to be constant from pulse to pulse, we expect that small variations in the surface area of the discharge will influence C_D values and thereby the peak I_R. As mentioned in table 3, the variance in C_D values is about 4% which would lead to about 1.5% extra error in peak I_R values. The time axis presented in the figure is the same as in figures 13 and 14 meaning that the 20 ns mark represents the time of peak V_T. As discussed above, plasma breakdown happens faster and the peak I_R value decreases from pulse to pulse for $d = 2$ mm and $d = 3$ mm. For thicker dielectrics, both values stay almost constant after the first pulse. This can be attributed to weaker pulse-to-pulse coupling and lesser gas heating. Moreover, peak I_R values for initial pulses are much lower than for later pulses which indicates weaker plasma ignition. Note that the dielectric thickness has a significant influence on I_R. Below, we will estimate the electron density (n_e) and the effective reduced electric field (E/N) at a peak I_R from OES.

Along with I_R, V_G is also important as it governs E/N and thereby the plasma kinetics. Mean values of V_G at the time of peak I_R are plotted for various dielectric thicknesses along with mean peak resistive powers P_R in figure 16. The mean V_G values vary between 14–18 kV for various thicknesses. The smallest value of about 14 kV is observed for 2 mm dielectric as breakdown happens on the rising edge of the applied voltage. Similar to peak I_R, the variation in surface discharge area from pulse-to-pulse would result in about 3% extra error in V_G on top of the standard deviations shown in the figure. Moreover, the mean peak P_R halves by increasing the thickness from 2 to 9 mm which is due to the decrease of the peak resistive current.

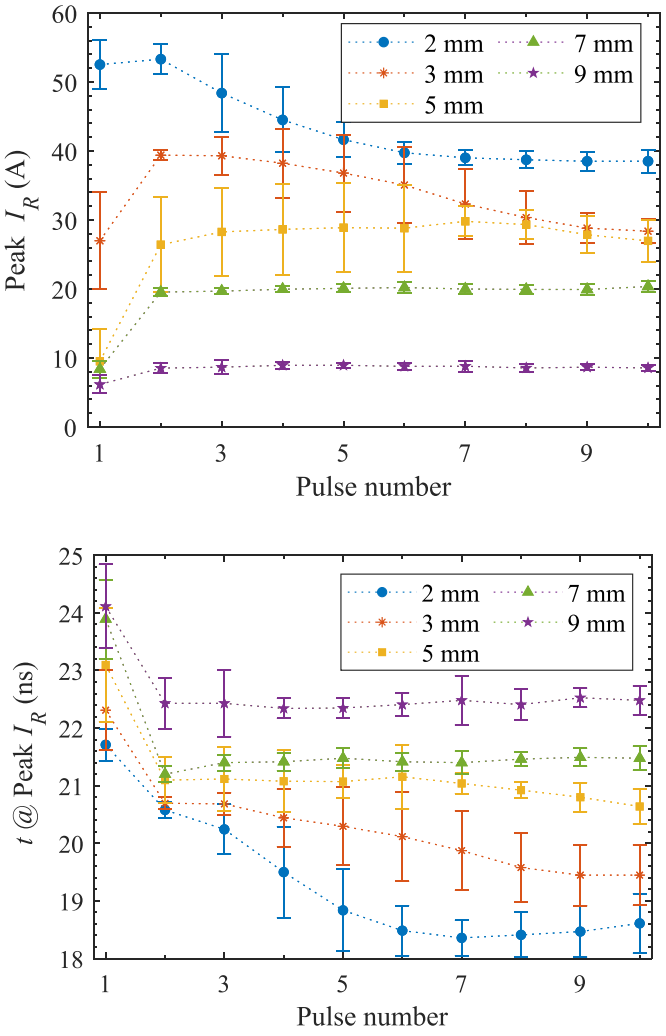

Figure 15. (a) Peak resistive current and (b) time of the current peak for various pulse numbers (n_p) and dielectric thicknesses (d) at $n_b = 10$ and $p = 700$ mbar. The applied voltage peaks at $t = 20$ ns.

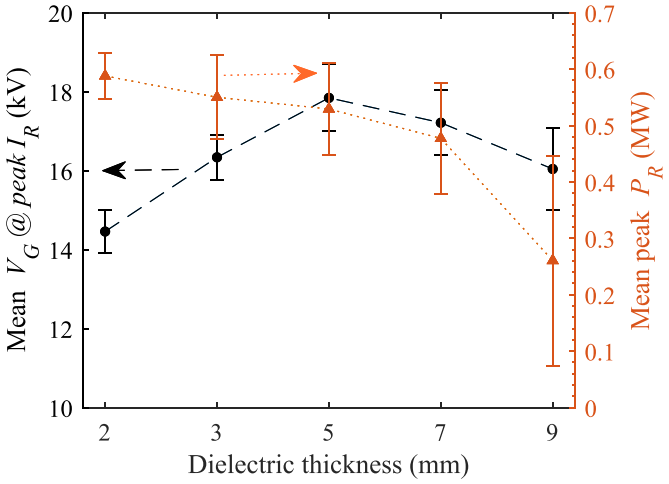

Figure 16. Mean voltage drop across gas gap (V_G) at peak resistive current (I_R) and mean peak resistive power for (P_R) for $n_b = 10$ and $p = 700$ mbar. Averaging is performed over 2 to 10 pulses.

4. Optical emission spectroscopy (OES)

Lastly, OES is performed to quantify the effect of dielectric thickness on plasma gas temperature and effective reduced electric field (E/N). Sample spectra and methods used for the estimations are described in section 2.2.3. Gas temperatures as function of pulse number for air and methane–air plasmas at 700 mbar are plotted in figure 17. At this pressure, OES is not possible for 9 mm dielectric because of the very weak plasma emissions.

In air, we observe a significant pulse-to-pulse temperature rise for $d = 2$ mm. The temperature during the fourth pulse is about 650 K which increases up to about 900 K at the seventh pulse. A similar trend is seen for $d = 3$ mm but at higher pulse numbers. The temperature reaches about 650 K during the seventh pulse, so three more pulses are needed compared to $d = 2$ mm. Almost no pulse-to-pulse gas heating is observed for $d = 5$ and 7 mm. These trends are consistent with the plasma morphology and peak I_R results discussed in the previous sections.

The temperature rises much faster in the methane–air mixture than in air. This indicates that combustion heat release provides a major contribution to the temperature rise in the combustible mixture. Only three pulses are needed to exceed 1000 K for $d = 2$ mm dielectric, indicating combustion ignition. Similarly, four pulses are needed for $d = 3$ mm even though more than five pulses are needed for significant pulse-to-pulse heating in air. This means that less plasma pulses are required for pulse-to-pulse coupling in a methane–air mixture than in air. This phenomenon is more visible for thicker dielectrics or cases with lower energy coupling per pulse because small heat addition from combustion heat release can have a significant influence on plasma morphology in these conditions. Rousso *et al* [62] have characterized this phenomenon and reported diffuse to filamentary mode transition in the presence of fuel. The results are attributed to temperature rise due to combustion heat release.

In figure 18, the development of E/N as function of pulse number for various dielectric thickness are plotted. It is quite evident that the development closely follows the gas temperature trends in air plasma. This can be attributed to the lower gas density (N) at higher temperatures. Note that E/N during the first pulse decreases with dielectric thickness. The first pulses of a burst occur in virgin gas at room temperature such that E/N depends only on V_G. From the equivalent circuit analysis we know that V_G is inversely proportional to the dielectric thickness. Hence, E/N is inversely related to the thickness for the first pulses. However, E/N is also governed by gas temperature for the rest of the pulses of the burst. That is why pulse-to-pulse E/N changes significantly for thinner dielectrics even though V_G is almost constant. Overall, it is clear that E/N estimations only from the equivalent circuit analysis (from V_T or V_G) can be misleading in such conditions.

Electron number density (n_e) can be estimated from

$$j = n_e \cdot e \cdot \mu \cdot N \cdot E/N, \tag{8}$$

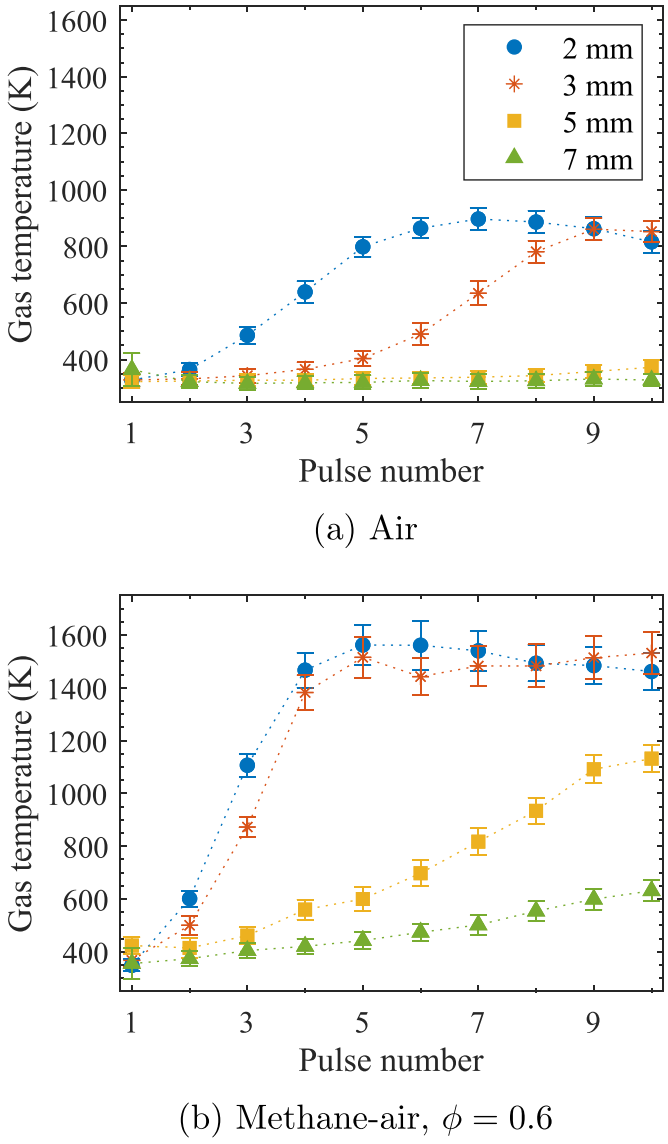

Figure 17. Gas temperature obtained from OES data for various pulse numbers, dielectric thicknesses, and $p = 700$ mbar in (a) air and (b) methane–air, $\phi = 0.6$.

where $j = I_R/(\pi D^2/4)$ is the current density, D the filament diameter, n_e the electron density, e the elementary charge, and μ the electron mobility. For the second pulse, 2 mm dielectric, and 700 mbar, $I_R = 48.4$ A (see figure 15(a)), $D = 0.36$ mm [48], $\mu N = 8.8 \cdot 10^{23}\,\mathrm{m^{-1}\,V^{-1}\,s^{-1}}$ [63, 64], and $E/N = 344$ Td (figure 18). This gives a peak $n_e = 9.7 \cdot 10^{15}$ $(\pm 8.1 \cdot 10^{15})$ $\mathrm{cm^{-3}}$ for the second pulse. The biggest uncertainty in this approach comes from the filament diameter (D) estimation which is assumed to be equal to the full width at half maximum of plasma light emission. Moreover, the estimated E/N is obtained from averaging the emission spectrum over the pulse duration and filament width. The real peak E/N will therefore be different from the reported effective value. Due to these uncertainties, we will not discuss the effects of dielectric thicknesses and pulse numbers on n_e. Advanced laser diagnostics such as Thomson scattering [65] or E-FISH [66, 67] can be used to reduce the uncertainties.

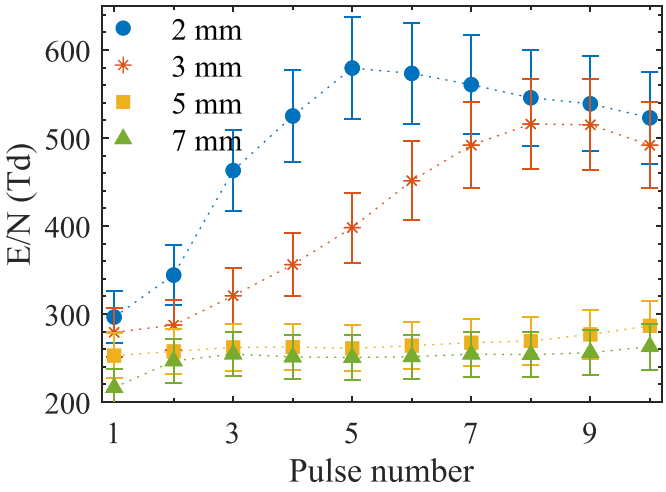

Figure 18. Effective reduced electric field obtained from OES data for various pulse numbers, dielectric thicknesses. All in $p = 700$ mbar air.

However, stabilizing the micro discharges at one location for plasma and laser interaction is also challenging.

5. Conclusions

We have investigated the effects of dielectric thickness on pulsed DBD plasma-assisted ignition of methane–air flows. We used a custom-built DBD reactor with one electrode covered with a dielectric, the thickness of which is varied. Experiments are performed in burst mode with various numbers of pulses per burst at a fixed 3 kHz PRR, 90 Hz burst frequency, and 1.5 m $\mathrm{s^{-1}}$ bulk flow speed.

From high-speed chemiluminescence visualization, we conclude that more pulses are required for thicker dielectrics to ignite the lean methane–air mixture with 0.6 equivalence ratio. For 9 mm thick dielectric, combustion ignition is not achieved at all even though plasma breakdown is observed. This phenomenon is further investigated by performing electrical and optical diagnostics of the discharge and important outcomes are the following: with an increase in dielectric thickness,

- the plasma energy per pulse decreases significantly and so more pulses are required to ignite lean methane–air flow hence slowing down the ignition kernel growth rate. *MIE* is found to be minimum for 3 mm thickness cases.
- the plasma remains longer distributed over multiple weak filaments which suggests weaker pulse-to-pulse plasma coupling. This can explain why the pulse-to-pulse gas heating is much lower for the thicker dielectrics.
- the effective dielectric capacitance (C_D) decreases, leading to a decrease in charge storing capacity and thereby in peak resistive current (I_R).
- the voltage drop across the gas gap (V_G) decreases and thereby the effective E/N during the first few pulses of a burst. However, during later pulses, the effective E/N is governed by pulse-to-pulse gas heating.

Lower *MIE* can be achieved by distributing ignition energy over multiple weaker pulses rather than using a few very strong pulses because radicals' production efficiency decreases drastically as equilibrium plasma transition occurs during a pulse. Experiments reported by Shen *et al* [68] indicate that MIE decreases non-linearly with coupled energy per pulse in NRP-operated pin-to-pin discharges. Mao *et al* [69] have simulated similar discharge conditions and reported lower ignition energy for double pulse ignition than a single pulse. Contrary, we observe an increase in *MIE* with an increase in dielectric thickness for more than 3 mm because the plasma energy density is too low to achieve significant pulse-to-pulse coupling. Overall, we conclude that, in order to achieve pulsed DBD plasma-assisted ignition at near atmospheric conditions, there exists a cut-off coupled energy per pulse at which plasma non-equilibrium efficiency and pulse-to-pulse coupling can be optimized.

Data availability statement

All data that support the findings of this study are included within the article (and any supplementary files).

ORCID iDs

Ravi Patel https://orcid.org/0000-0002-0117-3339
Jeroen van Oijen https://orcid.org/0000-0002-4283-2898
Sander Nijdam https://orcid.org/0000-0002-1310-6942

References

[1] Ju Y and Sun W 2015 Plasma assisted combustion: dynamics and chemistry *Prog. Energy Combust. Sci.* **48** 21–83
[2] Turns S R 2000 *An Introduction to Combustion: Concepts and Applications* (McGraw-Hill)
[3] Starikovskiy A and Aleksandrov N 2013 Plasma-assisted ignition and combustion *Prog. Energy Combust. Sci.* **39** 61–110
[4] Hazenberg T, van Dijk J and van Oijen J A 2023 Chemical flux analysis of low-temperature plasma-enhanced oxidation of methane and hydrogen in argon *Combust. Flame* **257** 113037
[5] Do H, Cappelli M A and Mungal M G 2010 Plasma assisted cavity flame ignition in supersonic flows *Combust. Flame* **157** 1783–94
[6] Matsubara Y, Takita K and Masuya G 2013 Combustion enhancement in a supersonic flow by simultaneous operation of DBD and plasma jet *Proc. Combust. Inst.* **34** 3287–94
[7] Takita K, Murakami K, Nakane H and Masuya G 2005 A novel design of a plasma jet torch igniter in a scramjet combustor *Proc. Combust. Inst.* **30** 2843–9
[8] Tian Y, Zhu J, Sun M, Wang H, Huang Y, Feng R, Yan B, Sun Y and Cai Z 2023 Enhancement of blowout limit in a Mach 2.92 cavity-based scramjet combustor by a gliding arc discharge *Proc. Combust. Inst.* **39** 5697–705
[9] Barbosa S, Pilla G, Lacoste D A, Scouflaire P, Ducruix S, Laux C O and Veynante D 2015 Influence of nanosecond repetitively pulsed discharges on the stability of a swirled propane/air burner representative of an aeronautical combustor *Phil. Trans. R. Soc.* A **373** 61–110
[10] Mintoussov E I, Pendleton S J, Gerbault F G, Popov N A and Starikovskaia S M 2011 Fast gas heating in nitrogen–oxygen discharge plasma: II. Energy exchange in the afterglow of a volume nanosecond discharge at moderate pressures *J. Phys. D: Appl. Phys.* **44** 285202
[11] Di Sabatino F, Guiberti T F, Moeck J P, Roberts W L and Lacoste D A 2020 Actuation efficiency of nanosecond repetitively pulsed discharges for plasma-assisted swirl flames at pressures up to 3 bar *J. Phys. D: Appl. Phys.* **54** 075208
[12] Paulauskas R, Martuzevičius D, Patel R B, Pelders J E H, Nijdam S, Dam N J, Tichonovas M, Stri = ugas N and Zakarauskas K 2020 Biogas combustion with various oxidizers in a nanosecond DBD microplasma burner *Exp. Therm. Fluid Sci.* **118** 110166
[13] Brandenburg R 2017 Dielectric barrier discharges: progress on plasma sources and on the understanding of regimes and single filaments *Plasma Sources Sci. Technol.* **26** 053001
[14] Gibalov V I and Pietsch G J 2012 Dynamics of dielectric barrier discharges in different arrangements *Plasma Sources Sci. Technol.* **21** 024010
[15] Kogelschatz U 2003 Dielectric-barrier discharges: their history, discharge physics and industrial applications *Plasma Chem. Plasma Process.* **23** 1–46
[16] Shao T, Jiang H, Zhang C, Yan P, Lomaev M I and Tarasenko V F 2013 Time behaviour of discharge current in case of nanosecond-pulse surface dielectric barrier discharge *Europhys. Lett.* **101** 45002
[17] Massines F, Ghérardi N, Naudé N and Ségur P 2009 Recent advances in the understanding of homogeneous dielectric barrier discharges *Eur. Phys. J. Appl. Phys.* **47** 22805
[18] Starostin S A, Premkumar P A, Creatore M, Van Veldhuizen E M, de Vries H, Paffen R M J and van de Sanden M C M 2009 On the formation mechanisms of the diffuse atmospheric pressure dielectric barrier discharge in CVD processes of thin silica-like films *Plasma Sources Sci. Technol.* **18** 045021
[19] Bílek P, Kuthanová L, Hoder T and Šimek M 2022 Atmospheric pressure townsend discharge in pure nitrogen—a test case for $\mathbf{N}_2(\mathbf{A}^3\sigma_u^+, v)$ kinetics under low E/N conditions *Plasma Sources Sci. Technol.* **31** 084004
[20] Seri P, Wright A, Shaw A, Iza F, Bandulasena H, Borghi C A and Neretti G 2019 Influence of the voltage waveform's shape and on-time duration on the dissolved ozone produced by a DBD bubble reactor *Plasma Sources Sci. Technol.* **28** 035001
[21] Cahyani M R, Zuhaela I A, Saraswati T E, Anwar M, Suselo Y H andIsmayenti L 2021 Time dependence of the concentration of dissolved ozone in water generated by dielectric barrier discharge (DBD) plasma using atmospheric air *J. Phys.: Conf. Ser.* **1912** 012008
[22] Ozkan A, Dufour T, Bogaerts A and Reniers F 2016 How do the barrier thickness and dielectric material influence the filamentary mode and CO_2 conversion in a flowing DBD? *Plasma Sources Sci. Technol.* **25** 045016
[23] Brune L, Ozkan A, Genty E, de Bocarmé T V and Reniers F 2018 Dry reforming of methane via plasma-catalysis: influence of the catalyst nature supported on alumina in a packed-bed DBD configuration *J. Phys. D: Appl. Phys.* **51** 234002
[24] Nakaya S, Yamaki Y, Ren F and Tsue M 2021 Effects of the discharge frequency on the dielectric barrier discharge ignition behaviors for lean methane–air mixtures at various pressure values *Combust. Flame* **234** 111650
[25] Shcherbanev S A, Stepanyan S A, Popov N A and Starikovskaia S M 2015 Dielectric barrier discharge for multi-point plasma-assisted ignition at high pressures *Phil. Trans. R. Soc.* A **373** 20140342

[26] Kim G T, Yoo C, Chung S H and Park J 2020 Effects of non-thermal plasma on the lean blowout limits and CO/NO_x emissions in swirl-stabilized turbulent lean-premixed flames of methane/air *Combust. Flame* **212** 403–14
[27] Vincent-Randonnier A, Larigaldie S, Magre P and Sabel'nikov V 2006 Plasma assisted combustion: effect of a coaxial DBD on a methane diffusion flame *Plasma Sources Sci. Technol.* **16** 149
[28] Elkholy A, Shoshyn Y, Nijdam S, van Oijen J A, van Veldhuizen E M, Ebert U and de Goey L P H 2018 Burning velocity measurement of lean methane-air flames in a new nanosecond DBD microplasma burner platform *Exp. Therm. Fluid Sci.* **95** 18–26
[29] Huiskamp T 2020 Nanosecond pulsed streamer discharges part I: generation, source-plasma interaction and energy-efficiency optimization *Plasma Sources Sci. Technol.* **29** 023002
[30] Nijdam S, Teunissen J and Ebert U 2020 The physics of streamer discharge phenomena *Plasma Sources Sci. Technol.* **29** 103001
[31] Pai D Z, Lacoste D A and Laux C O 2010 Transitions between corona, glow and spark regimes of nanosecond repetitively pulsed discharges in air at atmospheric pressure *J. Appl. Phys.* **107** 093303
[32] Rusterholtz D L, Lacoste D A, Stancu G D, Pai D Z and Laux C O 2013 Ultrafast heating and oxygen dissociation in atmospheric pressure air by nanosecond repetitively pulsed discharges *J. Phys. D: Appl. Phys.* **46** 464010
[33] Zhao Z, Li C, Zheng X, Sun A and Li J 2022 Periodical discharge regime transitions under long-term repetitive nanosecond pulses *Plasma Sources Sci. Technol.* **31** 045005
[34] Minesi N, Stepanyan S, Mariotto P, Stancu G D and Laux C O 2020 Fully ionized nanosecond discharges in air: the thermal spark *Plasma Sources Sci. Technol.* **29** 085003
[35] Pancheshnyi S V, Lacoste D A, Bourdon A and Laux C O 2006 Ignition of propane–air mixtures by a repetitively pulsed nanosecond discharge *IEEE Trans. Plasma Sci.* **34** 2478–87
[36] Lovascio S, Ombrello T, Hayashi J, Stepanyan S, Xa D, Stancu G D and Laux C O 2017 Effects of pulsation frequency and energy deposition on ignition using nanosecond repetitively pulsed discharges *Proc. Combust. Inst.* **36** 4079–86
[37] Lefkowitz J K and Ombrello T 2017 An exploration of inter-pulse coupling in nanosecond pulsed high frequency discharge ignition *Combust. Flame* **180** 136–47
[38] Shcherbanev S A, Malé Q, Dharmaputra B, Solana-Pérez R and Noiray N 2022 Effect of plasma-flow coupling on the ignition enhancement with non-equilibrium plasma in a sequential combustor *J. Phys. D: Appl. Phys.* **55** 425202
[39] Cathey C D, Tang T, Shiraishi T, Urushihara T, Kuthi A and Gundersen M A 2007 Nanosecond plasma ignition for improved performance of an internal combustion engine *IEEE Trans. Plasma Sci.* **35** 1664–8
[40] Shiraishi T, Urushihara T and Gundersen M 2009 A trial of ignition innovation of gasoline engine by nanosecond pulsed low temperature plasma ignition *J. Phys. D: Appl. Phys.* **42** 135208
[41] Singleton D, Pendleton S J and Gundersen M A 2010 The role of non-thermal transient plasma for enhanced flame ignition in C_2H_4–air *J. Phys. D: Appl. Phys.* **44** 022001
[42] Shcherbanev S A, Ding C, Starikovskaia S M and Popov N A 2019 Filamentary nanosecond surface dielectric barrier discharge. Plasma properties in the filaments *Plasma Sources Sci. Technol.* **28** 065013
[43] Lou G, Bao A, Nishihara M, Keshav S, Utkin Y G, Rich J, Lempert W R and Adamovich I V 2007 Ignition of premixed hydrocarbon–air flows by repetitively pulsed, nanosecond pulse duration plasma *Proc. Combust. Inst.* **31** 3327–34
[44] Bao A, Utkin Y G, Keshav S, Lou G and Adamovich I V 2007 Ignition of ethylene–air and methane–air flows by low-temperature repetitively pulsed nanosecond discharge plasma *IEEE Trans. Plasma Sci.* **35** 1628–38
[45] Lefkowitz J K, Uddi M, Windom B C, Lou G and Ju Y 2015 *In situ* species diagnostics and kinetic study of plasma activated ethylene dissociation and oxidation in a low temperature flow reactor *Proc. Combust. Inst.* **35** 3505–12
[46] Patel R, van Oijen J, Dam N and Nijdam S 2023 Low-temperature filamentary plasma for ignition-stabilized combustion *Combust. Flame* **247** 112501
[47] Patel R, Oommen C and Thomas M J 2020 Influence of reduced electric field (E/N) on plasma-assisted low-temperature oxidation *J. Propuls. Power* **36** 235–47
[48] Patel R, van Oijen J, Nijdam S and Dam N 2023 On pulse-to-pulse coupling in low-temperature filamentary plasma-assisted ignition in methane-air flows *Plasma Sources Sci. Technol.* **32** 065003
[49] Huiskamp T, Beckers F J C M, van Heesch E J M and Pemen A J M 2016 B-dot and D-dot sensors for (sub)nanosecond high-voltage and high-current pulse measurements *IEEE Sens. J.* **16** 3792–801
[50] Pipa A V and Brandenburg R 2019 The equivalent circuit approach for the electrical diagnostics of dielectric barrier discharges: the classical theory and recent developments *Atoms* **7** 14
[51] Liu S and Neiger M 2001 Excitation of dielectric barrier discharges by unipolar submicrosecond square pulses *J. Phys. D: Appl. Phys.* **34** 1632
[52] Lomaev M I 2001 Determination of energy input in barrier discharge excilamps *Atmos. Ocean. Opt.* **14** 1005–8
[53] Pipa A V, Hoder T, Koskulics J, Schmidt M and Brandenburg R 2012 Experimental determination of dielectric barrier discharge capacitance *Rev. Sci. Instrum.* **83** 075111
[54] Pipa A V, Koskulics J, Brandenburg R and Hoder T 2012 The simplest equivalent circuit of a pulsed dielectric barrier discharge and the determination of the gas gap charge transfer *Rev. Sci. Instrum.* **83** 115112
[55] Capitelli M, Ferreira C M, Gordiets B F and Osipov A I 2013 *Plasma Kinetics in Atmospheric Gases* vol 31 (Springer)
[56] Voráč J, Kusýn L and Synek P 2019 Deducing rotational quantum-state distributions from overlapping molecular spectra *Rev. Sci. Instrum.* **90** 123102
[57] Voráč J, Synek P, Potočňáková L, Hnilica J and Kudrle V 2017 Batch processing of overlapping molecular spectra as a tool for spatio-temporal diagnostics of power modulated microwave plasma jet *Plasma Sources Sci. Technol.* **26** 025010
[58] Paris P, Aints M, Valk F, Plank T, Haljaste A, Kozlov K V and Wagner H-E 2005 Intensity ratio of spectral bands of nitrogen as a measure of electric field strength in plasmas *J. Phys. D: Appl. Phys.* **38** 3894–9
[59] Nijdam S, Takahashi E, Markosyan A H and Ebert U 2014 Investigation of positive streamers by double-pulse experiments, effects of repetition rate and gas mixture *Plasma Sources Sci. Technol.* **23** 025008
[60] Li M, Li C, Zhan H, Xu J and Wang X 2008 Effect of surface charge trapping on dielectric barrier discharge *Appl. Phys. Lett.* **92**
[61] Cui G, Zeng W, Li Z, Fu Y, Li H and Chen J 2016 Experimental study of minimum ignition energy of methane/air mixtures at elevated temperatures and pressures *Fuel* **175** 257–63
[62] Rousso A C, Goldberg B M, Chen T Y, Wu S, Dogariu A, Miles R B, Kolemen E and Ju Y 2020 Time and space resolved diagnostics for plasma thermal-chemical instability of fuel oxidation in nanosecond plasma discharges *Plasma Sources Sci. Technol.* **29** 105012

[63] Hagelaar G J M and Pitchford L C 2005 Solving the Boltzmann equation to obtain electron transport coefficients and rate coefficients for fluid models *Plasma Sources Sci. Technol.* **14** 722
[64] Phelps A V and Pitchford L C 1985 Anisotropic scattering of electrons by $\mathbf{n}_2$ and its effect on electron transport *Phys. Rev.* A **31** 2932–49
[65] Carbone E and Nijdam S 2014 Thomson scattering on non-equilibrium low density plasmas: principles, practice and challenges *Plasma Phys. Control. Fusion* **57** 014026
[66] Chng T L, Orel I, Starikovskaia S M and Adamovich I V 2019 Electric field induced second harmonic (E-FISH) generation for characterization of fast ionization wave discharges at moderate and low pressures *Plasma Sources Sci. Technol.* **28** 045004
[67] Chng T L, Pai D Z, Guaitella O, Starikovskaia S M and Bourdon A 2022 Effect of the electric field profile on the accuracy of E-FISH measurements in ionization waves *Plasma Sources Sci. Technol.* **31** 015010
[68] Shen S, Laso I, Rozin N and Lefkowitz J K 2023 On pulse energy and energy distribution for ignition of flowing mixtures *Proc. Combust. Inst.* **39** 5487–98
[69] Mao X, Zhong H, Wang Z, Ombrello T and Ju Y 2023 Effects of inter-pulse coupling on nanosecond pulsed high frequency discharge ignition in a flowing mixture *Proc. Combust. Inst.* **39** 5457–64